

Microstructure modelling of high temperature micro-crack initiation and evolution in a welded 9Cr martensitic steel

M. Li¹, P. E. O'Donoghue¹, S. B Leen¹

¹*National University of Ireland Galway, Galway, Ireland*

Abstract: Welded joints in tempered 9Cr-1Mo operating at elevated temperatures are well known to be prone to premature failure due to cracking in the heat affected zone. This paper describes a crystal plasticity model to predict the micro-crack initiation and evolution in the inter-critical heat-affected (IC-HAZ) zone of 9Cr-1Mo welded steel at elevated temperature. A crystal plasticity finite element model indicates that the micro-cracks of 9Cr-1Mo steel mostly nucleate at prior austenite grain boundaries and boundary clustered regions. Inter-granular and trans-granular micro-cracking are shown to be the key predicted micro-damage mechanisms from the current crystal plasticity model. A small amount of ferrite in the IC-HAZ is shown to not only influence the micro-crack initiation and evolution, but also significantly accentuate material degradation for a given applied load leading to premature failure at high temperature.

Keywords: Crystal plasticity, weld, IC-HAZ, ferrite, crack nucleation and evolution

1. Introduction

Tempered 9Cr-1Mo martensitic steel is widely used in fossil fuel power plants for the main steam pipes, headers, boilers and other components, due to advantages such as high creep resistance and low thermal expansion at elevated temperature. These advantages enable 9Cr-1Mo steel to operate at super-critical working conditions, thus increasing the efficiency and reducing emissions [1, 2]. Welding is unavoidable in the construction of boilers for fossil fuel power plants [3]. Arising from the thermal history experienced in the welded region, particular microstructures are generated in a 9Cr-1Mo weld at specific sites as a result of a

decreasing prior austenite grain (PAG) size, illustrated in Fig. 1 [4]. The heat affected zones (HAZs) of a weld can be further sub-divided into three regions: coarse-grained HAZ (CG-HAZ), fine-grained HAZ (FG-HAZ) and the inter-critical HAZ (IC-HAZ) [5, 6]. For welds of 9Cr-1Mo steel at high temperature, the IC-HAZ region is the most common life-limiting region [7], where premature failure is commonly observed during service and testing, resulting in so-called Type-IV failure [6-8], for example.

The occurrence of IC-HAZ after welding is considered to be a serious problem for the long-term service of tempered 9Cr-1Mo steel welds in power plant [1, 8, 9] at elevated temperatures. Experimental investigations that compared the creep properties of 9Cr-1Mo steel welds with the parent metal at elevated temperature, demonstrated that creep resistance of the 9Cr welds is controlled by the IC-HAZ region [9, 10]. IC-HAZ has the lowest hardness in comparison with other regions of the welded joints after post weld heat treatment (PWHT) and after creep [1, 7]. The lower hardness of IC-HAZ after PWHT can be attributed to the partially un-dissolved precipitates during the heating cycle leading to the formation of coarse precipitates along the PAG boundary (PAGB) and low carbon content in the matrix during cooling [11, 12]. The existence of small amounts of pro-eutectoid ferrite in the IC-HAZ is reported in [13-15], which concluded that the low value of micro-hardness in IC-HAZ is due to the presence of this softer ferrite phase. The work of Abd El-Azim *et al.* [1] and Watanabe *et al.* [9] identified that reduced creep resistance of IC-HAZ is mainly because of the lower dislocation density of the IC-HAZ when compared with the parent material. .

A thorough understanding of the physical mechanisms of IC-HAZ cracking is necessary for detecting and preventing the failure of 9Cr-1Mo welds at elevated temperature [12, 16-18]. Baed on their micro-scale experiments, Xue *et al.* [16] claimed that cavities formed at the PAGB and block boundaries during creep due to coarse particles at the boundaries acting as the preferential nucleation sites for these cavities, and Li *et al.* [18] and Takashi *et al.* [9]

claimed that the cavities nucleated around the coarse particles in 9Cr-1Mo steel can be correlated with stress triaxiality. Kumar *et al.* [17] established that inter-granular triple-point cracking and the linking-up of cavities along the boundaries to form micro-cracks are responsible for the micro-damage in the IC-HAZ of 9Cr-1Mo welds. Lee and Maruyama [12] conducted microscopic investigations in order to obtain more details about the Type-IV cracking in IC-HAZ of 9Cr-1Mo welds. They found that IC-HAZ consists of a mixture of soft and hard grains, and this plays an important role in the process of cavity evolution into crack formation along the boundaries [1,12]. Park *et al.* and Yu *et al.* [19, 20] reported that the occurrence of ferrite in IC-HAZ of 9Cr-1Mo welds is correlated with the decohesion and micro-crack formation at grain boundaries under high temperature.

With the development of finite element (FE) approaches, different techniques, such as extended FE methods (XFEM), cohesive element methods and element deletion methods, have been adopted to assess the crack growth and damage evolution mechanisms for many materials [21-23, 25]. However, these computational approaches have their limitations in representing the detail of failure in microstructures. XFEM has been able to accurately predict crack propagation paths for many problems; however, it is still prone to numerical instabilities when treating non-linear constitutive responses [23]. Element deletion methods are extremely mesh sensitive and are not generally suitable for modelling failure with complex hierarchical morphologies [24]. Cohesive elements have been widely used to study inter-granular cracks but the crack path needs to be defined in advance [25]. It had been reported that crack growth in the IC-HAZ of 9Cr-1Mo welded steel is caused by the nucleation and growth of cavities at the boundary region with coarse Cr-rich $M_{23}C_6$ type precipitates, which subsequently coalesce as macroscopic cracks [12, 17]. The presence of grains and grain boundaries and other microstructural features cannot practically be taken into account using these approaches to

predict micro-crack growth and evolution. Therefore, it is important to identify the locations of damage nucleation with respect to microstructural features for martensite steel.

Crystal plasticity finite element (CPFE) approaches are very applicable for microstructure based predictions and much work had been carried out in the development of CPFE [18, 26-31]. A CPFE approach has been used to predict the locations of fatigue crack nucleation in FCC poly-crystal material showing good agreement with experimental observations [29]. A dislocation-density grain boundary interaction scheme has been developed and incorporated into a CPFE approach by Shanthraj and Zikry [30] to analyse crack nucleation and evolution based on the unique variant morphologies and inherent orientation relationships in martensitic microstructures; however, this work did not take the micro-structure dimension for a specific material into consideration in the modelling process. A CPFE approach was adopted by Tasan *et al.* [31] to deepen the understanding of the role of the microstructural parameters including crystallographic textures, crystallographic orientation and crystallographic size on the localized plastic behaviour and damage micro-mechanisms.

There has been limited study of how the crystallographic processes lead to failure mechanisms that depend on local grain and grain boundary orientations for IC-HAZ in 9Cr-1Mo welds. Thus damage modelling using CPFE approaches is an important area for future study. In this work, a CPFE approach coupled with a strain-controlled damage model is used to investigate the mechanical behaviour of 9Cr-1Mo welded material under monotonic tensile loading. The objective of the present study is to gain an understanding of the damage mechanisms in crack initiation and crack growth in 9Cr-1Mo welded steel by using an idealised microstructure mesh model within a CPFE analyses. Given the presence of ferrite in the IC-HAZ, it was important to assess its role in the failure process. Thus, the effect of a small volume fraction of ferrite and its orientations, on the global and local responses was investigated as well. To address these objectives two different models were created. In the first model, ferrite was not included and

this is referred to as single phase. However, in the second model, a small amount of ferrite [14], with different crystallographic orientations, was introduced for comparison and this is referred to as mixed-phase. In this work, the significance of a low volume fraction of ferrite in a martensite matrix on the microstructural deformation and the initiation of micro-cracks at high temperatures is investigated.

2. Methodology

2.1 Materials

The 9Cr-1Mo martensitic steel investigated in this work has a hierarchical microstructure as shown in Fig. 2. In this figure, the thick solid white lines indicate the PAGB or ferrite boundary, the thin solid lines are the packet boundaries and the dash lines are block boundaries. The martensite steel has a body-centred cubic (BCC) lattice structure consisting of packets, blocks, laths and precipitates. A collection of packets forms within a PAG and can be subdivided into blocks with inherent block orientation relationship containing laths [24]. Fig. 3 shows a scanning electron microscope (SEM) image of the IC-HAZ region from a sample of an ex-service 9Cr-1Mo weld. The microstructure of IC-HAZ in 9Cr-1Mo welds consists of small amounts of softer ferrite (highlighted in red) embedded in a martensite grain matrix (a number of these grains are highlighted in blue). Unlike the martensite, this ferrite does not have an internal microstructure (Fig. 2). This ferrite has been found to be about 5% by volume [14]. A similar crystallographic morphology for IC-HAZ in 9Cr-1Mo welds had already been reported in [13, 14, 16].

2.2 Micro-mechanical kinetic formulation for single crystal

The constitutive microstructure behaviour at the block level is represented by a rate dependent CPFEM model, accounting for elastic and plastic flow anisotropies for each block, without considering a size effect [32]. The crystal plasticity model adopted in the current work was initially developed by Busso and McClintock [33] and then other researchers used this crystal

plasticity model to investigate the micro-scale deformation for steel with FCC and BCC structures [15, 18, 34].

Following [26], the deformation gradient \mathbf{F} is decomposed into the two components, \mathbf{F}^e and \mathbf{F}^p , as follows:

$$\mathbf{F} = \mathbf{F}^e \mathbf{F}^p, \quad (1)$$

where \mathbf{F}^e is used to represent elastic deformation gradient due to the reversible response of the lattice to external loadings and rotation, while \mathbf{F}^p is an irreversible deformation gradient due to slip. With a slip system denoted as (\mathbf{m}, \mathbf{n}) , where \mathbf{m} is the unit vector in the slip direction and \mathbf{n} is the unit normal vector on the slip plane of the un-deformed lattice, the rate of plastic deformation, $\dot{\mathbf{F}}^p$ can be obtained from the following:

$$\dot{\mathbf{F}}^p \cdot \mathbf{F}^{p-1} = \sum_{\alpha=1}^N [\dot{\gamma}^{\alpha} \mathbf{m}^{\alpha} \otimes \mathbf{n}^{\alpha}], \quad (2)$$

$\dot{\gamma}^{\alpha}$ is the shear rate on slip system α , and N is the number of active slip systems for BCC structure. The inelastic slip rate on a slip system α , $\dot{\gamma}^{\alpha}$ is represented by a thermally activated flow rule [33] dependent on the resolved shear stress τ^{α} , as follows:

$$\dot{\gamma}^{\alpha} = \dot{\gamma}_0 \exp \left(-\frac{F_0}{kT} \left\langle 1 - \left\langle \frac{|\tau^{\alpha}| - S^{\alpha}}{\tau_0} \right\rangle^p \right\rangle^q \right), \quad (3)$$

In Eq. (3), T and k are absolute temperature and Boltzmann constant, respectively. The material constants are: F_0 , the total free activation energy needed to overcome the lattice resistance; τ_0 , the lattice friction stress at absolute temperature; p , q and $\dot{\gamma}_0$, are the exponents and pre-exponent constant, respectively. S^{α} represents a thermal component of the flow stress or overall slip resistance. τ^{α} is the resolved shear stress on a given slip system α , defined as follows:

$$\tau^{\alpha} = (\mathbf{F}^e)^T \mathbf{F}^e \mathbf{T}^* : (\mathbf{m}^{\alpha} \otimes \mathbf{n}^{\alpha}), \quad (4)$$

In Eq. (4) \mathbf{T}^* indicates the stress elastically work-conjugate to the elastic Green strain

$$\mathbf{T}^* = (\mathbf{F}^e)^{-1} J \boldsymbol{\sigma} \mathbf{T}^* (\mathbf{F}^e)^{-T}, \quad (5)$$

where $J = \det(\mathbf{F})$, $\boldsymbol{\sigma}$ and $J\boldsymbol{\sigma}$ are the Cauchy and Kirchhoff stress, respectively. The evolution of slip resistance S^α in Eq. (3) is defined as,

$$\dot{S}^\alpha = \sum_{\beta=1}^N h^{\alpha\beta} \left(\frac{S_{sat} - S^\beta}{S_{sat} - S_0} \right) |\dot{\gamma}^\beta|, \quad (6)$$

where $h^{\alpha\beta}$ in Eq. (6) is the hardening matrix and S_{sat} is the saturated slip resistance with initial value S_0 . The hardening matrix, $h^{\alpha\beta}$, can be written as

$$h^{\alpha\beta} = h_s \left[\omega_1 + (1 - \omega_2) \delta_{\alpha\beta} \right], \quad (7)$$

where h_s is a material constant for all slip systems (active and inactive) and $\delta_{\alpha\beta}$ is the Kronecker delta. The slip resistance $h^{\alpha\beta}$ depends not only on the active slip systems α (self-hardening) but also on the non-active slip system β (latent hardening), through the constants ω_1 and ω_2 [34]. If $\omega_1 = 1$, $\omega_2 = 1$ all slip systems harden equally, irrespective of whether active or not, leading to isotropic crystallographic hardening (Taylor hardening, [35].)

2.3 Cauchy-Lorentz function for micro-damage model

The accumulated equivalent plastic strain (ε_{eq}^{pl}) has been proposed by a number of authors as an important indicator parameter for crack initiation. In this paper, we adopt a strain-controlled damage progression model in conjunction with micro-plasticity in order to describe the localized deformation. This damage model has previously been applied for austenitic stainless to account for damage development. The accumulated equivalent plastic strain ε_{eq}^{pl} is defined as:

$$\varepsilon_{eq}^{pl} = \int_0^t \left(\frac{2}{3} \mathbf{D}^p : \mathbf{D}^p \right)^{\frac{1}{2}} dt, \quad (8)$$

where t is the current simulation time and \mathbf{D}^p is plastic strain rate tensor, expressed as:

$$\mathbf{D}^p = \frac{1}{2} \sum_{\alpha=1}^N \gamma^\alpha \left[\mathbf{F}^e \mathbf{m}^\alpha \otimes \mathbf{n}^\alpha (\mathbf{F}^e)^{-1} + (\mathbf{F}^e)^{-T} \mathbf{n}^\alpha \otimes \mathbf{m}^\alpha (\mathbf{F}^e)^T \right] \quad (9)$$

A microstructural damage variable, ω , varying from 0 (no damage) to 1 (fully damage), is adopted to describe the degradation of the elastic stiffness. The modified local elastic stiffness matrix is written as follows:

$$\mathbf{C} = \mathbf{C}_0 (1 - \omega), \quad (10)$$

where \mathbf{C}_0 is the material elastic stiffness without damage. A continuously varying ω is assumed using a modified Cauchy-Lorentz cumulative distribution function as follows:

$$\omega = 1 + \left[\frac{1}{2} + \frac{1}{\pi} \arctan\left(\frac{\varepsilon_c}{d}\right) \right]^{-1} \left[\frac{1}{\pi} \arctan\left(\frac{\varepsilon_{eq}^{pl} - \varepsilon_c}{d}\right) - \frac{1}{2} \right]. \quad (11)$$

The Cauchy-Lorentz function in Eq. (11) provides a phenomenological description of a damage transition with $\omega = 0$ at $\varepsilon_{eq}^{pl} \leq 0$ and $\omega \rightarrow 1$ as $\varepsilon_{eq}^{pl} \rightarrow \varepsilon_c$ and ε_c is the critical strain. Here d is a measure of the damage transition region and is taken to be 0.1. Fig. 4 gives the variation of ω , which indicates the damage evolution for different values of the critical failure strain, ε_c . The material model defined in Section 2.2 was first implemented by Busso and McClintock [33] and the damage model in Section 2.3 was first implemented by Li and O'Dowd [36] in a material user subroutine (UMAT) in the non-linear commercial finite-element code ABAQUS [37].

2.4. IC-HAZ parameters identification

2.4.1 Morphological representation and boundary conditions

To reflect the microstructure morphology of the polycrystalline aggregates of martensite grain with internal microstructure, a modified Voronoi Tessellation (VT) method was created comprising of 444 blocks distributed within 80 packets for a total of 20 PAGs following the approach in Li *et al.* [15, 38]. The corresponding FE model is shown in Fig. 5 with the internal microstructure details in a representative volume element (RVE), which illustrates the topology

of Voronoi columnar PAG and blocks both possessing a mean grain size of 10 μm [2] and block width of approximately 1.5 μm [39], respectively. As described in detail by Sun *et al.* [38], the measured Euler angles of the microstructure in 9Cr-1Mo steel can be represented by the Kurdjumow–Sachs (K–S) relationship [40], so that the crystallographic information in the FE model exactly matches the measured electron backscatter diffraction (EBSD) results [38]. The second Euler angles are used to represent crystallographic orientations in the poly-crystal FE model. The inverse pole figure gives the initial crystallographic orientations used in the FE model, which indicates that 9Cr-1Mo steel has a uniform crystal orientation distribution. Note that the dimension of the RVE is appropriate such that a representative macroscopic response can be obtained using the poly-crystal FE model as shown in the earlier study [41]. Periodic boundary conditions in the out-of-plane direction are imposed on the two dimensional RVE model incorporated through the use of 3D elements (C3D8 in ABAQUS) to reflect the spatial periodicity of deformations in an infinitely large body.

2.4.2 Mesh sensitivity study and material parameters identification

The single-phase model (no ferrite included) is utilised here in the first instance to conduct mesh sensitivity studies and for fitting the IC-HAZ data to obtain the material parameters at elevated temperatures. Since the FE predictions may depend on the mesh refinement, a mesh sensitivity study is conducted to investigate the rate of convergence of the VT model. The number of elements ranged from about 12,500 to 63,000 with average element size ranging from 0.04 μm to 0.089 μm . Fig. 6 illustrates the mesh for the RVE with 30,600 elements.

Tensile test data for IC-HAZ was measured by Touboul *et al.* [42] from an ex-service 9Cr-1Mo weld through digital image correlation (DIC) testing at 625 °C. Fig. 7(a) shows a comparison of the experimental data for IC-HAZ with a strain-rate of $1.0 \times 10^{-3}/\text{s}$, represented by symbols, and the corresponding predictions from the RVE, with different numbers of elements shown as solid lines. It can be seen that at lower strain levels (<4%), prior to the accumulation of

damage, the computed results are independent of mesh size. The maximum macroscopic stress of 280 MPa is accurately captured by the model. As one of the main objectives in this study is to investigate micro-crack initiation and evolution, it is important to ensure that the predicted failure strain ε_f converges for these micro-damage studies. A 20% load drop is chosen to represent the failure condition and this is consistent with the experimental data in Fig. 7(a). It can be clearly seen that the failure strain decreases at increasing levels of mesh refinement. From Fig. 7(b), it is evident that the failure strain (based on the 20% load drop) converges when the number of elements is 30,600. Thus, the 30,600-element mesh with average element size 0.057 μm is used in the subsequent finite-element VT analysis. The material parameters used in the crystal plasticity model for IC-HAZ are listed in Table 1 and Table 2. In the experimental work by Touboul *et al.* [42], testing was carried out at three different strain rates, namely 10^{-3} , 10^{-4} and $10^{-5}/\text{s}$. The strain-rate effect on flow stress for IC-HAZ at 625 °C is reasonably captured through the current CPFEM model by using this set of constants, as shown in Fig. 8.

3. Results

3.1 Micro-crack initiation and evolution for single phase.

The multiple-slip crystal plasticity formulation and the representation of cracks using a modified damage model were used to investigate the microstructural failure of martensitic steel. σ_{yy} and equivalent plastic strain distributions (ε_{eq}^{pl}) at 3.8% macroscopic strain, which is just before the onset of micro-crack nucleation, are shown in Figs. 9(a) and (b) for a strain rate of $10^{-3}/\text{s}$ where the loading is aligned along the axial y direction. The non-uniform nature of σ_{yy} and ε_{eq}^{pl} is primarily caused by the differing distributions of crystal orientations. The average predicted σ_{yy} in Fig. 9(a) is approximately 280 MPa. The computed results show a complex pattern of stress due to the orientation mismatch between neighbouring blocks with local stress concentrations zones forming in some regions. The maximum micro-stress concentration factor is ~ 1.5 relative to the global response. The blocks showing stress

concentrations in Fig. 9(a) do not generally exhibit higher localized ε_{eq}^{pl} , and these higher strain areas have lower stresses as seen in Fig. 9(b). In contrast, the strain is more concentrated at the vicinity of boundary regions, as shown in Fig. 9(b). It can be inferred that for 9Cr-1Mo steel, the boundary regions are more detrimental with respect to localized strain concentrations.

In this work, the accumulation of damage and the formation of micro-cracks and their subsequent growth towards failure are ultimately controlled by the localized strain state. Fig. 9(c) provides the damage contour plot with the elongation at 3.8% strain (without PAG and block boundaries for the purpose of clarity) in order to show the micro-crack initiation regions. Note that the damage scale in Fig. 9(c) has been selected to more clearly illustrate the micro-crack locations. Six different micro-crack nucleation regions are highlighted and these are consistent with regions of localised strain (Fig. 9(b)). These regions are illustrated in Fig. 10, giving greater clarity of the crack nucleation sites relative to the PAG and block boundaries. The predicted micro-crack nucleation results illustrate that the micro-cracks nucleate around PAG-packet-block boundaries or PAG-block boundaries as summarized in Table 3. Note that the micro-crack nucleation regions predicted by the CPFE model are independent on the mesh. Kumar *et al.* [17] reported that micro-cracks have been observed experimentally both in the PAGB regions and in the triple junctions through SEM images and this is consistent with the results predicted numerically in this work. Since IC-HAZ regions in 9Cr-1Mo welds contains super-fine PAG ($\sim 10 \mu\text{m}$) compared with other regions, i.e. $351 \mu\text{m}$ for CG-HAZ after PWHT [13], higher boundary density of IC-HAZ than other regions in the welds can result in more micro-damage nucleation possibilities according to the predicted micro-crack nucleation results in the current work. The occurrence of coarse particles, i.e. M_{23}C_6 , along boundaries will assist the formation of cavities in IC-HAZ [12, 16]. The interaction of these two factors would be detrimental for the generation of premature failure in 9Cr-1Mo welds at elevated temperature.

The evolution of damage and its effect on crack growth in martensite steel is already recognized as a complex phenomenon, owing to the inherent microstructural inhomogeneity with the prior martensitic substructure [9]. Therefore, it is interesting to observe the micro-crack growth for the single-phase first. For this distribution, the initiation of the micro-cracks occurs mainly at PAGB (Fig. 10), as a result of the local strain concentrations due to the favourable orientation of the cleavage planes in contiguous blocks.

The crack propagation paths as the strain is further increased to 4.5% and then 5.5% are illustrated in Figs 11(a) and (b), respectively. The dominant micro-cracks align along the high-angle boundary and along favourably oriented cleavage planes across the adjacent block. The fracture mechanism is determined by the competition between large strain concentrations along high-angle boundaries, due to the accumulation of strain, and the favourable orientation of cleavage planes in blocks. Fig. 12 provides the details of two main micro-crack paths corresponding to the micro-crack paths in Fig. 11(b). Two fracture mechanisms are predicted by the current CPFEM model, inter-granular to trans-granular for path-1 and trans-granular for path-2. Similar intergranular and transgranular fracture mechanisms have also been reported in previous experimental work for low carbon martensite steel [43].

3.2 Micro-crack initiation and evolution for mixed phase.

Small amounts of ferrite can be seen in the IC-HAZ region after welding [13, 14]. Although the single-phase martensite model has been calibrated (in Fig. 7) to correlate closely to the measured IC-HAZ stress-strain data at 625°C, on the assumption of no ferrite phase, the purpose of the mixed-phase model is to investigate the stress-strain and inhomogeneity of local micro-cracking behaviour as a result of the inclusion of such a softer ferritic phase. Micro-hardness indentation tests for the ferrite and martensite phases in the IC-HAZ of 9Cr-1Mo welds demonstrated a hardness value for martensite of approximately 1.25 times that of the ferrite phase [44]. Fig. 13(a) illustrates the approach with an isolated ferrite grain embedded

within the martensite matrix. Two important orientations are chosen for the single crystal ferrite grain based on previous studies by the authors [15], $\langle 100 \rangle$ orientation which exhibits a softer response and $\langle 110 \rangle$ orientation which shows a slightly harder crystallographic response. The corresponding mixed-phase FE model is shown in Fig. 13(b) and includes the ferritic phase (5% by volume) which does not have the same internal microstructure as the martensite grains. The martensite grains in the mixed phase model have the identical orientations to those in the single phase case (Fig. 9(a)).

For calibration purposes, the single phase result (all martensite) has been shown in Fig. 7(a) at 625 °C with the measured IC-HAZ data from [42]. A result showing similar agreement at 20 °C was shown in previous work [15]. Figs 14(a) and (b) present the comparison of the single-phase with two mixed-phase analyses containing ferrite with $\langle 100 \rangle$ and $\langle 110 \rangle$ orientations at temperatures of 20 °C and 625 °C, respectively. It can be seen from Fig. 14(a) that the effect of ferrite (with either orientation) is not particularly significant with a negligible effect on hardening and a relatively similar effect on strain to failure in each case. In contrast, at 625 °C, the effect of the ferrite grain is much more significant, with considerable softening exhibited by the mixed-phase for both ferrite orientations, leading to significant material degradation compared with the single-phase response. It can also be seen that the strain to failure (based on the 20% load drop) is also greatly influenced by the ferrite grain and the crystallographic orientation. The softer $\langle 100 \rangle$ gives a more severe reduction than the slightly harder $\langle 110 \rangle$. The comparison of predicted single-phase tensile responses with mixed-phase at 20 °C and 625 ° is summarized in Table 4. Therefore, the mixed-phase model predicts that a small amount of ferrite will accelerate the material degradation in IC-HAZ at high temperature, leading to failure of 9Cr-1Mo welds at lower bulk stress.

Fig. 15 shows the prediction of micro-crack evolution for the single-phase and mixed-phase with the different ferrite orientations at 625 °C. The 20% load drop is again used here as the

criterion for strain at failure and the damage evolutions at those three corresponding strains are plotted here. A larger RVE in the left for each image is based on periodic boundary condition in order to understand the trend of micro-crack propagation for the three cases. It can be clearly seen that the micro-crack and damage patterns are significantly changed when the ferrite is included. The micro-crack initiation and evolution is very much dependent on the local grain crystallographic orientations and the grain morphology. For the ferrite with the softer $\langle 100 \rangle$ orientation (Fig. 14(b)), there is a significant decrease in the material ductility of about 13.2% compared to the single-phase predicted response, since micro-cracks can grow across inter-ferrite ligaments with large damage accumulating in this softer ferrite. This can influence the softening rate, leading to material degradation at lower loads. The micro-cracks for the mixed-phase with the $\langle 100 \rangle$ ferrite nucleates at the PAGB due to strain concentration and then penetrates into the ferrite region with significant strain along the crack path with the micro-cracking mechanism transitioning from intergranular to transgranular, as shown in Fig. 15(b). Furthermore, micro-cracks are also observed at the boundaries of the ferrite grain leading to de-cohesion, which is in agreement with the experimental work of Park *et al.* [19], who confirmed that micro-cracks easily nucleate at soft δ -ferrite grain boundaries in 9Cr-1Mo steel. As shown in Fig. 15(c), the ferrite grain with the harder $\langle 110 \rangle$ orientation acts as an obstacle to micro-crack growth compared with Fig. 15(b), leading to negligible reduction in ductility (see Table 4), but an obvious effect on softening. However, this orientation can lead to greater damage due to a stronger interactive effect with the surrounding blocks. It had been reported in previous work by the authors [15] that the $\langle 110 \rangle$ ferrite grain further accentuates the ε_{eq}^{pl} concentration in the most highly strained block location, relative to the original single-phase martensite microstructure. In this case, the micro-cracks distribute around the ferrite grain. It was reported by Yu *et al.* [20] that micro-cracks and voids were also found to be located around the ferrite grain regions in 9Cr-1Mo welded steel. Note that similar micro-crack mechanisms

are predicted by the current CPFEM approach for both single-phase and mixed-phase at 20 °C and 625 °C, respectively. However, more slip systems will be activated due to the availability of sufficient free activation energy at high temperature to overcome the lattice resistance, leading to more damage accumulation and further promoting the micro-crack nucleation and growth. The introduction of ferrite grain at high temperature can significantly accentuate the material softening as reflected in the global response.

4. Conclusion and discussion

Crystal plasticity modelling with damage has been presented for poly-crystalline martensite steel at 625 °C and compared to the corresponding results for 20 °C. An RVE, consisting of a number of martensite grains with the K-S orientation relationship and a small amount of specifically orientated ferrite grain, has been constructed using the modified VT and meshed for FE analyses under periodic boundary constraints. The model parameters were determined from DIC test data at 625 °C using a fitting process. Simulations using fitted parameters showed agreement with experimental data. A particular focus of this work was on the IC-HAZ region in the welds as this can be the location for the onset of premature cracking. These studies can be summarised by the following conclusions:

1. Mesh sensitivity studies for a CPFEM model established an appropriate level of refinement and comparison with experimental data led to the implementation of a 20% load drop criterion as an indicator of strain to failure.
2. The strain rate effect of IC-HAZ at 625 °C was successfully predicted by the current crystal plasticity model.
3. More slip systems are likely to be activated at 625°C, leading to additional plastic slip and further increasing the damage accumulation in the poly-crystal material compared to the corresponding results at 20°C. A small amount of ferrite can promote the micro-crack nucleation and accelerate the material degradation in IC-HAZ at high

temperature, leading to weld failure at lower loads, which is detrimental to the integrity of 9Cr-1Mo welded steel pipes.

4. The CPFE model demonstrated that micro-cracks in welded 9Cr-1Mo steel generally initiate at the PAGB and boundary clustered regions, which is consistent with experimental observations. Inter-granular and trans-granular micro-cracking modes were predicted for 9Cr-1Mo steel by the crystal plasticity model.
5. Predicted results show that the ferrite phase in 9Cr-1Mo welded steels leads to a reduced strength at high temperatures and also plays an important role on micro-crack initiation and evolution. Ferrite grains with a 'soft' orientation are prone to causing crystal decohesion at the ferrite boundary.
6. Since IC-HAZ contains super-fine PAG compared with other regions in 9Cr-1Mo welds, higher boundary densities of IC-HAZ than other regions in the welds probably results in more micro-damage nucleation possibilities. More work needs to be done for the statistical boundary effect within each specific region of 9Cr-1Mo welds on micro-crack nucleation and the global response, i.e. the material uniaxial response, fatigue behaviour, and creep life, to deepen our understanding of failure in 9Cr-1Mo welds at elevated temperature. From one grain to another, the individual grain size and orientation contribute to how easy or how difficult it is for micro-cracks to develop. Thus, the effects of ferrite grain size and orientation, ferrite grain distribution and the presence of ferrite in the IC-HAZ of 9Cr-1Mo welds are also deserving of investigation in the future work, as these factors are critical to the localized plastic behaviour, damage micro-mechanisms and the influence the material ductility.

Acknowledgements

This publication has emanated from research conducted with the financial support of Science Foundation Ireland under Grant No. 14/IA/2604 and the College of Engineering and Informatics at NUI Galway. The authors are grateful to the Irish Center for High-End Computing (ICHEC) for supporting the computational work (uleng040b). Helpful discussions with the Mechannics team (NUI Galway and UL). The assistance of Mr Edward Meade of the Bernal Institute at UL is also gratefully acknowledged. The 9Cr-1Mo welded material was provided by Mr. Stephen Scully of Electricity Supply Board (ESB International). Mr. Scully also provided helpful insight into the operation of conventional power plant and the metallurgy of martensitic steels.

References:

1. Abd El-Azim, M.E., O.H. Ibrahim, and O.E. El-Desoky (2013). “Long term creep behaviour of welded joints of P91 steel at 650°C”. *Materials Science and Engineering: A*. **560**: p. 678-684.
2. Abe, F., M. Tabuchi, M. Kondo and S. Tsukamoto (2007). “Suppression of Type-IV fracture and improvement of creep strength of 9Cr steel welded joints by boron addition.” *International Journal of Pressure Vessels and Piping* **84**(1-2): 44-52.
3. Viswanathan, R., J. F. Henry, J. Tanzosh, G. Stanko, J. Shingledecker, B. Vitalis and R. Purgert (2005). “U.S. Program on Materials Technology for Ultra-Supercritical Coal Power Plants.” *Journal of Materials Engineering and Performance* **14**(3): 281-292.
4. Indacochea, J.E., Wang, G., Seshadri, R., “Creep rupture properties of high-temperature Bainitic steels after weld repair,” (2000). *Journal of Engineering Material and Technology*, **122**, 259-263.
5. Mayr, P. and H. Cerjak, (2010). “The impact of welding on the creep properties of advanced 9-12% Cr steels.” *Transactions of the Indian Institute of Metals*, **63**(2-3): p. 131-136.
6. Francis, J.A., W. Mazur, and H.K.D.H. Bhadeshia, (2013). “Review Type IV cracking in ferritic power plant steels,” *Materials Science and Technology*, **22**(12): p. 1387-1395.

7. Laha, K., K. S. Chandravathi, P. Parameswaran, K. B. S. Rao and S. L. Mannan (2007). "Characterization of microstructures across the heat-affected zone of the modified 9Cr-1Mo weld joint to understand its role in promoting Type-IV Cracking." *Metallurgical and Materials Transactions A*, **38**(1): 58-68.
8. Albert, S.K., Albert, S. K., Matsui, M., Watanabe, T., Hongo, H., Kubo, K., Tabuchi, M., (2002). "Microstructural investigations on Type-IV cracking in a high Cr steel," *Isij International*, **42**(12): p. 1497-1504.
9. Watanabe, T., M. Tabuchi, M. Yamazaki, H. Hongo and T. Tanabe, (2006). "Creep damage evaluation of 9Cr-1Mo-V-Nb steel welded joints showing Type-IV fracture." *International Journal of Pressure Vessels and Piping* **83**(1): 63-71.
10. Tabuchi, M., Watanabe, T., Kubo, K., Matsui, M., Kinugawa, J., Abe, F., (2001) "Creep crack growth behavior in the HAZ of weldments of W containing high Cr steel," *International Journal of Pressure Vessels and Piping*, **78**(11-12): p. 779-784.
11. Divya, M., Das, C.R., Albert, S.K., Goyal, S., Ganesh, P., Kaul, R., Swaminathan, J., Murtyd, B.S., Kukreja, L.M. and Bhaduria, A.K., (2014), "Influence of welding process on Type-IV cracking behaviour of P91 steel," *Materials Science & Engineering A*, **613**, 148-158
12. Lee, J.S. and K. Maruyama, (2015), "Mechanism of Microstructural Deterioration Preceding Type IV Failure in Weldment of Mod.9Cr-1Mo Steel," *Metals and Materials International*, **21**(4): p. 639-645.
13. Pandey, C., Giri, A., Mahapatra, M. M., Kumar, P., (2017), "Characterization of Microstructure of HAZs in As-Welded and Service Condition of P91 Pipe Weldments," *Metals and Materials International*, **23**(1): p. 148-162
14. Paul, V. T., S. Saroja, P. Hariharan, A. Rajadurai and M. Vijayalakshmi (2007). "Identification of microstructural zones and thermal cycles in a weldment of modified 9Cr-1Mo steel." *Journal of Materials Science* **42**(14): 5700-5713.
15. Li, M., Sun, F.W., Li, D.F., PE O'Donoghue, NP O'Dowd, SB Leen, (2018) "The effect of ferrite phases on the micromechanical response and crack initiation in the inter-critical heat-affected zone of a welded 9Cr martensitic steel", *Fatigue & Fracture of Engineering Materials & Structures*, **41**(6): 1245-1259.
16. Xue, W., Q.-g. Pan, Y.-y. Ren, W. Shang, H.-q. Zeng and H. Liu (2012). "Microstructure and type-IV cracking behavior of HAZ in P92 steel weldment." *Materials Science and Engineering: A* **552**: 493-501.
17. Kumar, Y., Venugopal, S., Sasikala, G., Albert, Shaju K., Bhaduri, A. K., (2016). "Study of creep crack growth in a modified 9Cr-1Mo steel weld metal and heat affected zone", *Materials Science and Engineering: A*, **655**: p. 300-309.
18. Li D.F., Barrett R.A., O'Donoghue P., O'Dowd N.P., Leen S.B., (2017). "A multi-scale crystal plasticity model for cyclic plasticity and low-cycle fatigue in P91 steel at elevated temperature." *Journal of the Mechanics and Physics of Solids*, **101**, 44-62.

19. Park, J.S., S.J. Kim, and C.S. Lee, (2001). "Effect of W addition on the low cycle fatigue behavior of high Cr ferritic steels", *Materials Science and Engineering A*, **298**(1-2): p. 127-136.
20. Yu, X., Babu, S. S., Terasaki, H., Komizo, Y., Yamamoto, Y., Santella, M. L., (2013). "Correlation of precipitate stability to increased creep resistance of Cr–Mo steel welds," *Acta Materialia*, **61**(6): p. 2194-2206.
21. Martinez, J.C., L.V.V. Useche, and M.A. Wahab, (2017). "Numerical prediction of fretting fatigue crack trajectory in a railway axle using XFEM," *International Journal of Fatigue*, **100**: p. 32-49.
22. Needleman, A., (2014). "Some issues in cohesive surface modeling," *Mechanics for the World: Proceedings of the 23rd International Congress of Theoretical and Applied Mechanics, Ictam2012*, **10**: p. 221-246.
23. Song, J.H., H.W. Wang, and T. Belytschko, (2008). "A comparative study on finite element methods for dynamic fracture," *Computational Mechanics*, **42**(2): p. 239-250.
24. Morito, S., H. Tanaka, R. Konishi, T. Furuhashi and T. Maki (2003). "The morphology and crystallography of lath martensite in Fe-C alloys." *Acta Materialia* **51**(6): 1789-1799.
25. Wells, G.N. and L.J. Sluys, (2001). "A new method for modelling cohesive cracks using finite elements," *International Journal for Numerical Methods in Engineering*, **50**(12): p. 2667-2682.
26. Asaro, R.J. and Rice. J.R, (1977). "Strain localization in ductile single crystals," *Journal of Mechanics and Physics Solids*, **25**, 309–38.
27. Anand, L. and M. Kothari, (1996). "A computational procedure for rate-independent crystal plasticity," *Journal of the Mechanics and Physics of Solids*, **44**(4): p. 525-558.
28. McGinty, R.D. and D.L. McDowell, (2006). "A semi-implicit integration scheme for rate independent finite crystal plasticity," *International Journal of Plasticity*, **22**(6): p. 996-1025.
29. Dunne, F.P.E., A.J. Wilkinson, and R. Allen, (2007). "Experimental and computational studies of low cycle fatigue crack nucleation in a polycrystal," *International Journal of Plasticity*, **23**(2): p. 273-295.
30. Shanthraj, P. and M.A. Zikry, (2013). "Microstructurally induced fracture nucleation and propagation in martensitic steels," *Journal of the Mechanics and Physics of Solids*, **61**(4): p. 1091-1105
31. Tasan, C.C., Hoefnagels, J. P. M., Diehl, M., Yan, D., Roters, F., Raabe, D., (2014). "Strain localization and damage in dual phase steels investigated by coupled in-situ deformation experiments and crystal plasticity simulations," *International Journal of Plasticity*, **63**: p. 198-210.
32. Ghassenmi-Armaki, H., Maab, R., Bhat, S.P., Sriram, S., Greer, J.R. and Kumar, K.S., "Deformation response of ferrite and martensite in a dual-phase steel," *Acta Materialia*, **62**(2014), 197-211.

33. Busso, E.P. and F.A. McClintock, (1996). "A dislocation mechanics-based crystallographic model of a B₂-type intermetallic alloy," *International Journal of Plasticity*, **12**(1): p. 1-28.
34. Li, D. F. and N. P. O'Dowd (2011). "On the evolution of lattice deformation in austenitic stainless steels-The role of work hardening at finite strains." *Journal of the Mechanics and Physics of Solids*, **59**(12): 2421-2441.
35. Taylor, G. I. (1934). "The Mechanism of Plastic Deformation of Crystals. Part I. Theoretical." *Proceedings of the Royal Society of London. Series A, Containing Papers of a Mathematical and Physical Character*, **145**(855): 362-387.
36. Li, D. F., C. M. Davies, S. Y. Zhang, C. Dickinson and N. P. O'Dowd (2013). "The effect of prior deformation on subsequent microplasticity and damage evolution in an austenitic stainless steel at elevated temperature." *Acta Materialia* **61**(10): 3575-3584.
37. ABAQUS V6.11. Providence (RI): Hibbitt, Karlsson and Sorensen, 2011.
38. Sun, F.W., E.D. Meade, and N.P. O'Dowd, (2018). "Microscale modelling of the deformation of a martensitic steel using the Voronoi tessellation method," *Journal of the Mechanics and Physics of Solids*, **113**: p. 35-55.
39. Wang, Y., R. Kannan and L. Li (2016). "Characterization of as-welded microstructure of heat-affected zone in modified 9Cr-1Mo-V-Nb steel weldment." *Materials Characterization*, **118**: 225-234.
40. Kitahara, H., R. Ueji, N. Tsuji and Y. Minamino (2006). "Crystallographic features of lath martensite in low-carbon steel," *Acta Materialia*, **54**(5): 1279-1288.
41. Li, M., F. W. Sun, R. A. Barrett, E. Meade, D. F. Li, P. E. O'Donoghue, S. B. Leen and N. P. O'Dowd (2017). "Influence of material inhomogeneity on the mechanical response of a tempered martensite steel." *Proceedings of the Institution of Mechanical Engineers Part L-Journal of Materials-Design and Applications*, **231**(1-2): 14-22.
42. Touboul, M., J. Crepin, G. Rousselier, F. Latourte and S. Leclercq (2013). "Identification of local viscoplastic properties in P91 welds from full field measurements at room temperature and 625 °C," *Experimental Mechanics*, **53**(3): 455-468.
43. Krauss, G., (1995). "Heat-Treated Martensitic Steels - Microstructural Systems for Advanced Manufacture," *Isij International*, **35**(4): p. 349-359.
44. Hsiao, T. H., T. C. Chen, S. L. Jeng, T. J. Chung and L. W. Tsay (2016). "Effects of Simulated Microstructure on the Creep Rupture of the Modified 9Cr-1Mo Steel," *Journal of Materials Engineering and Performance* **25**(10): 4317-4325.

Tables:

Table 1: Elastic constants and flow rule parameters used in the poly-crystal model (625 °C).

C_{11} (GPa)	C_{22} (GPa)	$C_{44}(\mu)$ (GPa)	$\dot{\gamma}_0$ (s^{-1})	p (-)	q (-)	F_0 (J)	τ_{0m} (MPa)
98.14	65.7	90.2	0.01	0.5	1.25	0.43×10^{-18}	220

Table 2: Strain hardening and damage parameters used in the poly-crystal model (625 °C).

S_0 (MPa)	S_{sat} (MPa)	h_s (MPa)	ω_1 (-)	ω_2 (-)
2.2	250	520	1	1

Table 3: Summary of PAG and block boundary details at the micro-crack nucleation regions

Nucleation location	Micro-crack nucleation	boundary details at the nucleation region
1	PAGB	PAG-block-packet boundary junction
2	PAGB	PAG boundary
3	PAGB	PAG-block-packet boundary junction
4	PAGB	PAG-block-packet boundary junction
5	PAGB	PAG-block boundary
6	PAGB	PAG-block boundary

Table 4: Comparison of predicted single-phase tensile results with mixed-phase at 20 °C and 625 °C

Method	Ultimate strength, 20 °C (MPa)	Ductility 20 °C (%)	Ultimate strength, 625 °C (MPa)	Ductility 625 °C (%)
CPFE-single phase	615	9.0	285.8	6.64
CPFE-mixed phase: <100> ferrite	590	9.3	262.6	5.85
CPFE-mixed phase: <110> ferrite	600	8.5	271.4	6.35

Figures:

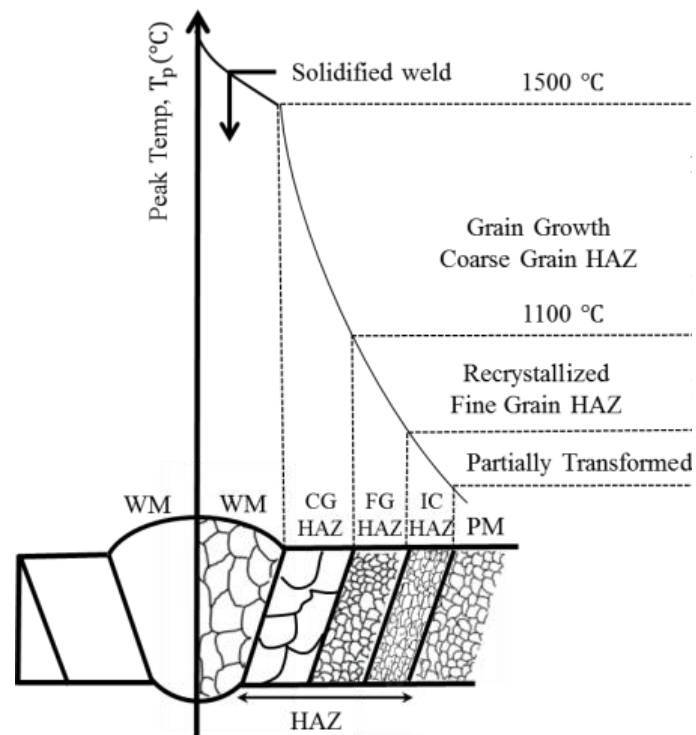


Fig. 1: A schematic of the weld regions as corresponding to the equilibrium Fe-C binary phase diagram adapted from [4].

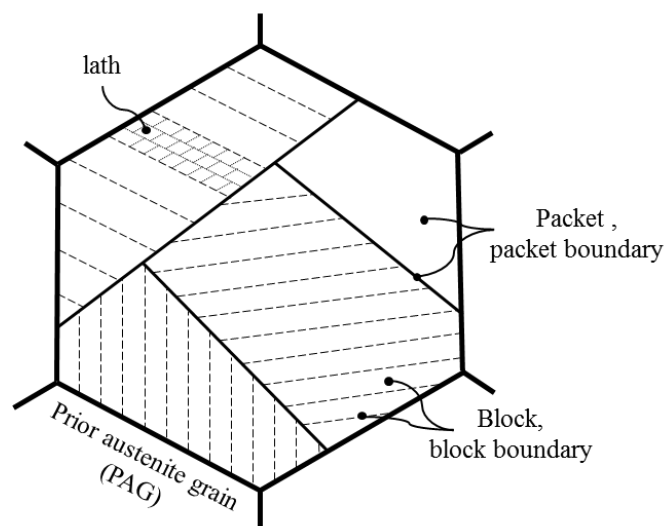


Fig. 2: Schematic illustration of the hierarchical microstructure in 9Cr-1Mo martensitic steel including PAG, packet, block and lath.

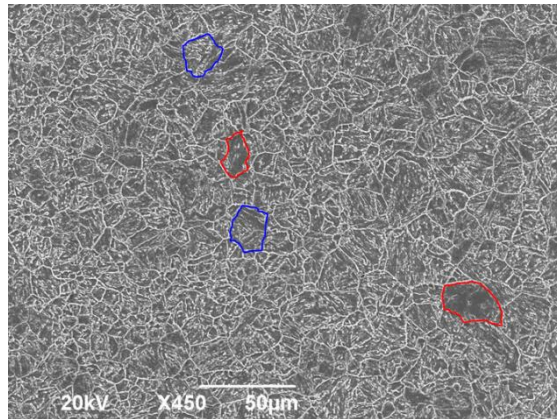


Fig. 3: SEM image of the IC-HAZ region from ex-service 9Cr-1Mo welds consisting of small amount of soft ferrite (highlighted with red lines) and martensite (highlighted with blue).

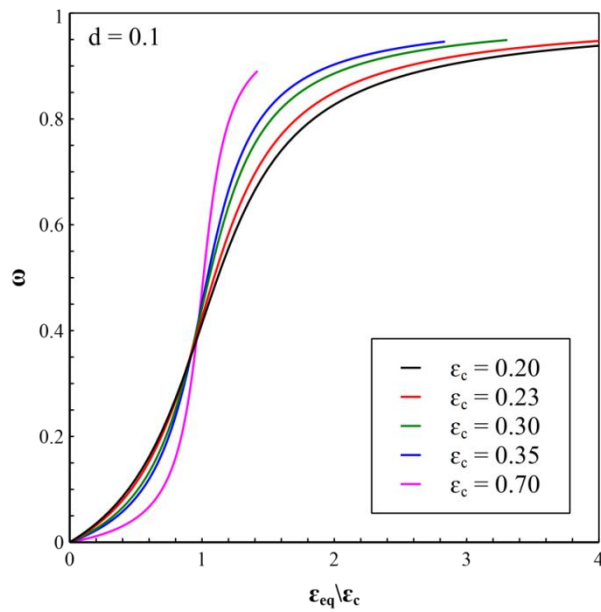


Fig. 4: Comparison of damage evolution based on Cauchy-Lorentz cumulative distribution function for different sets of constants critical strain values.

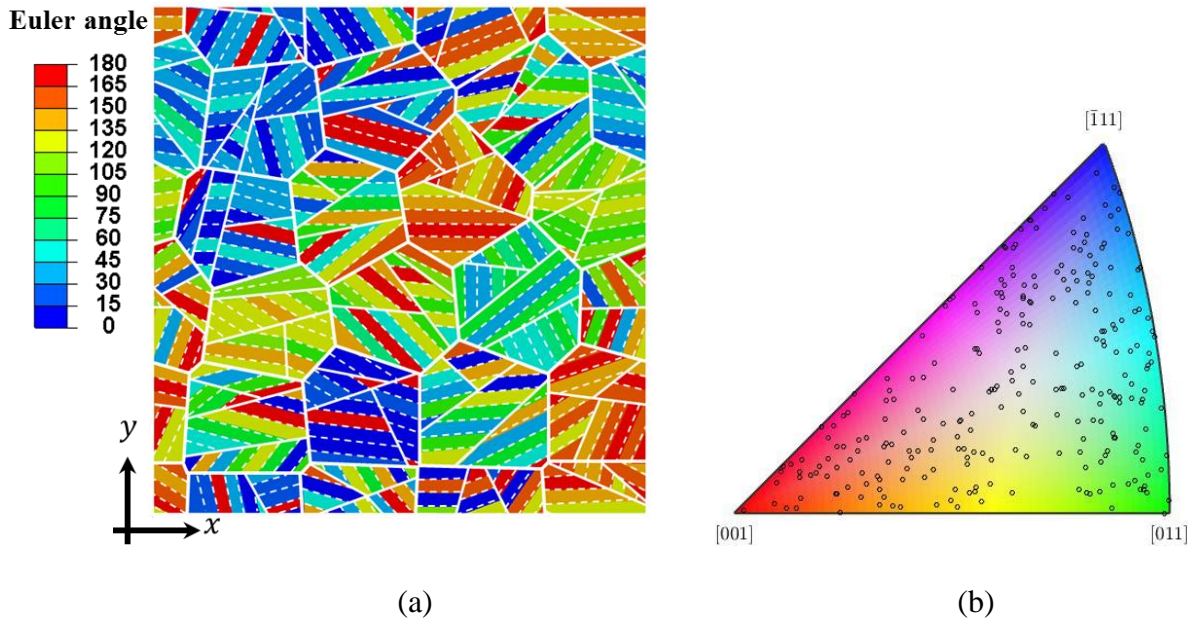


Fig. 5: (a) Micro-mechanical finite element model for IC-HAZ (single-phase) in 9Cr welds;
 (b) The spatial distribution of the second Euler angle from Fig. 5(a).

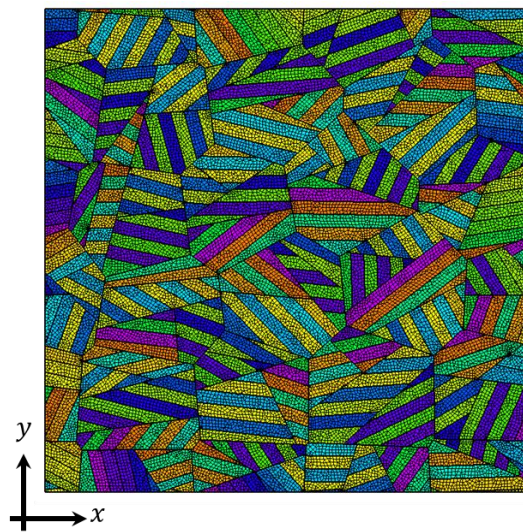


Fig. 6: Example of mesh for the single-phase model with 30,600 elements.

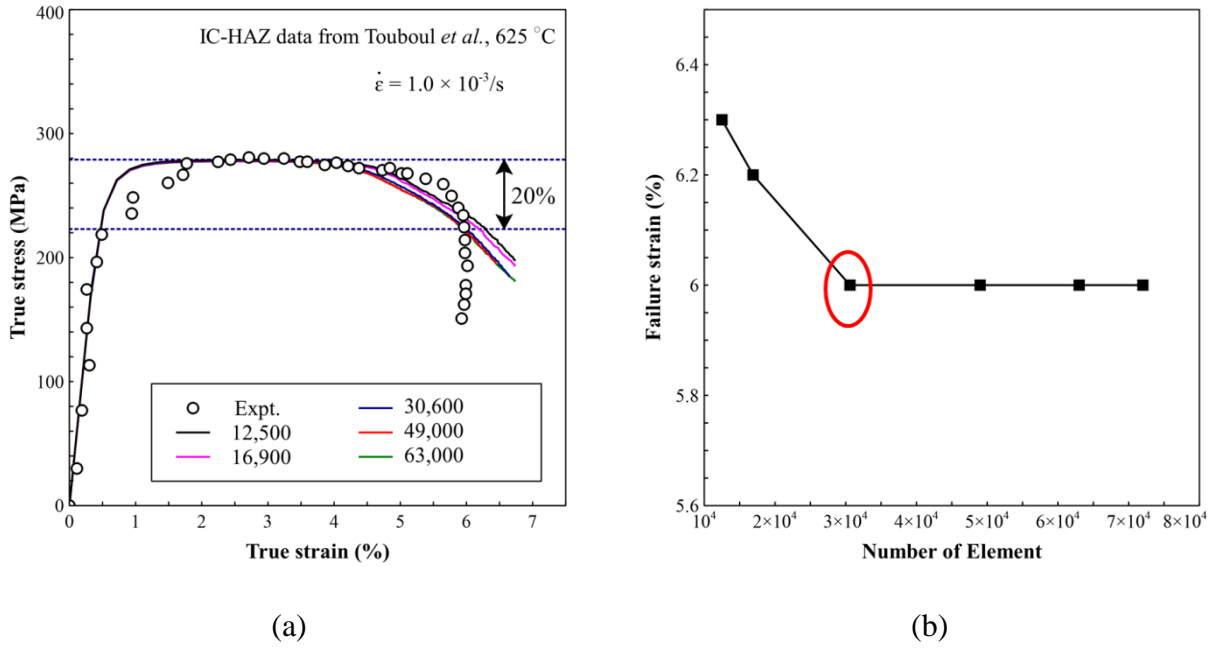


Fig. 7: (a) Single phase used here with different numbers of elements for sensitivity study until failure; (b) Effect of number of elements on 20% drop load failure strain.

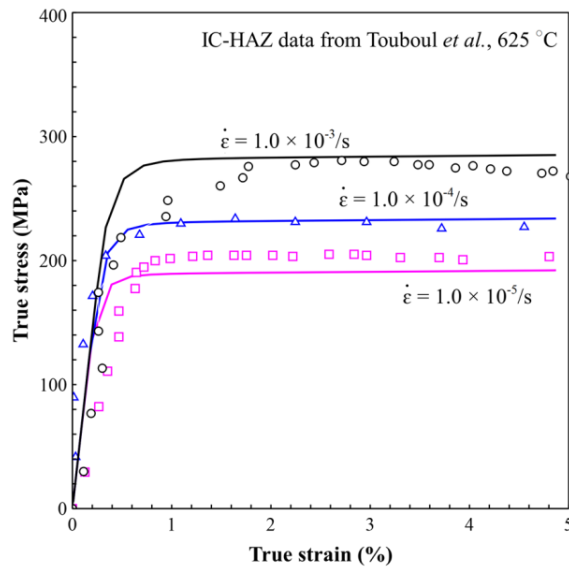


Fig. 8: Prediction of strain-rate effect for IC-HAZ at 625°C; IC-HAZ data is from [41] through DIC testing.

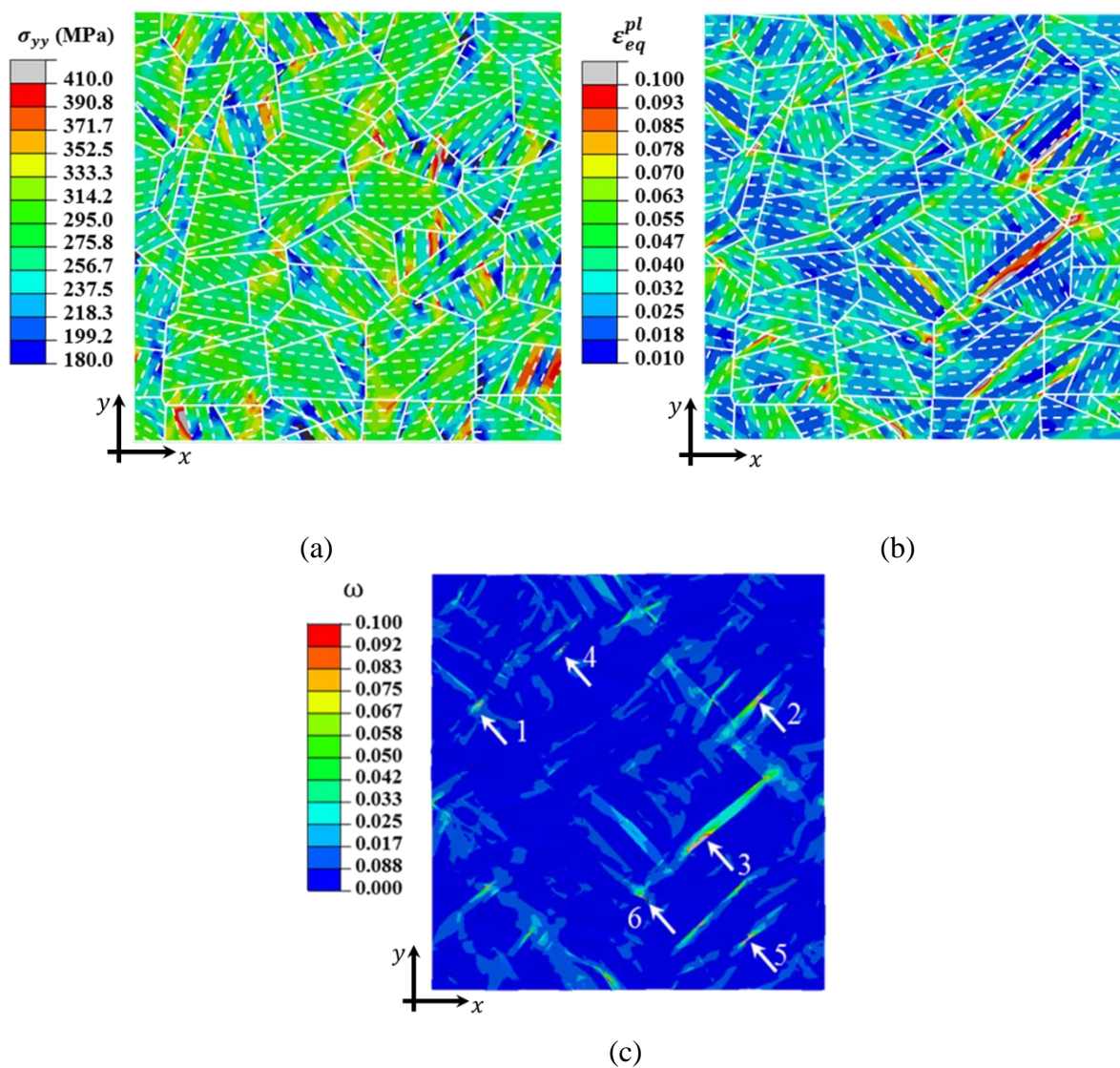


Fig. 9: (a) σ_{yy} distribution (b) ε_{eq}^{pl} distribution and (c) Damage contour plot, showing multiple sites of micro-crack nucleation at 3.8% strain and $10^{-3}/s$ strain-rate.

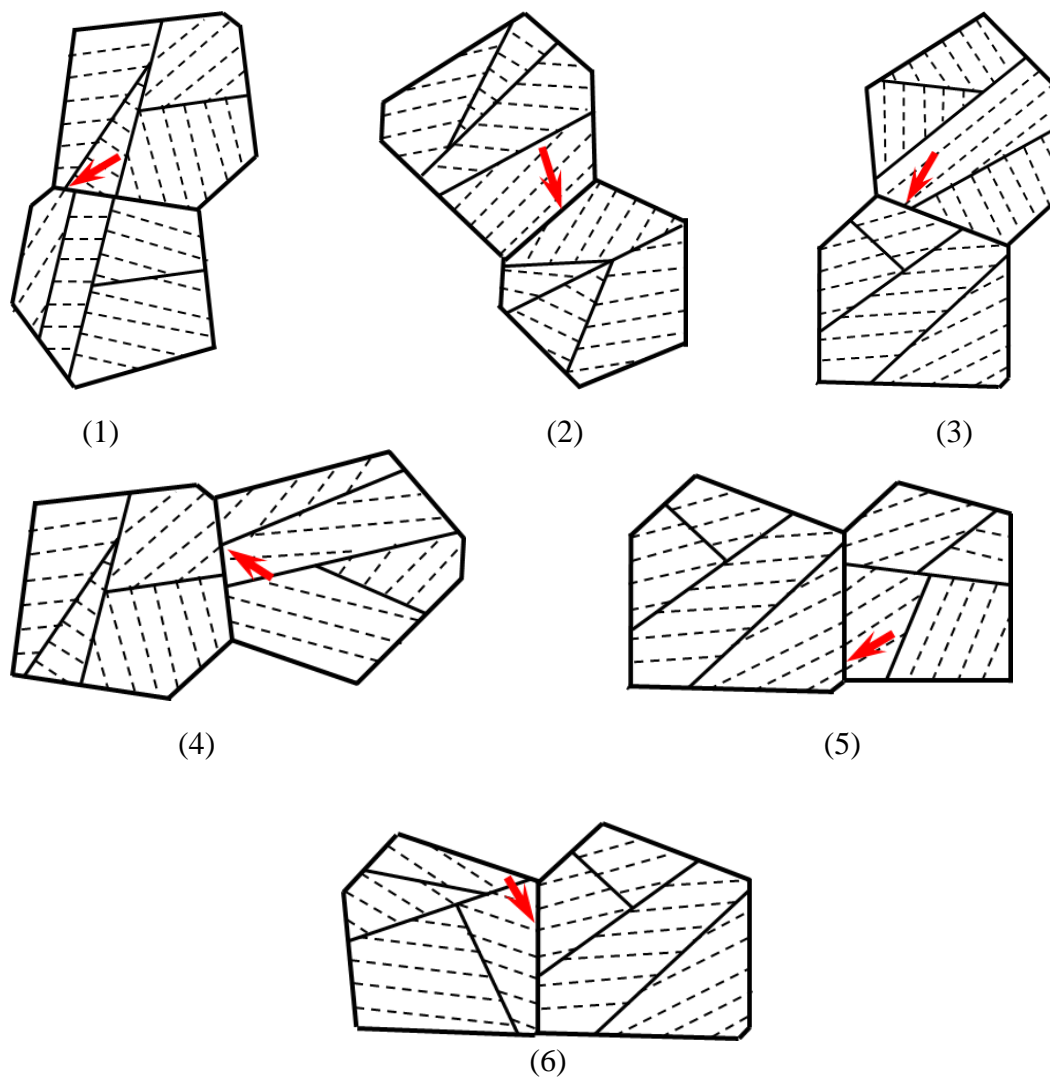


Fig. 10: PAG and block boundaries at the micro-crack nucleation regions corresponding to Fig. 9(c).

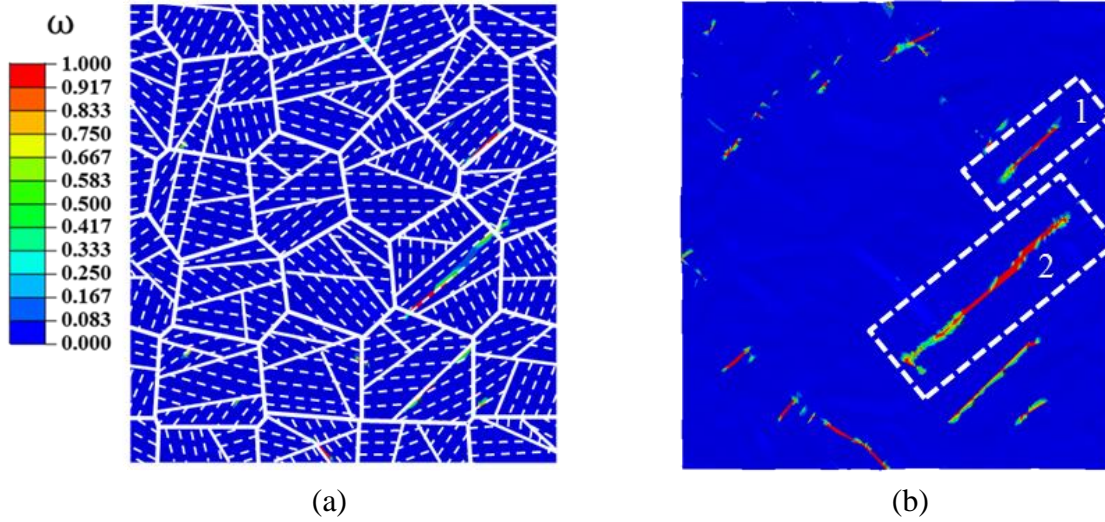


Fig. 11: Micro-crack evolution for single phase as the strain is at (a) 4.5%, (b) 5.5% at 10^{-3} /s strain-rate.

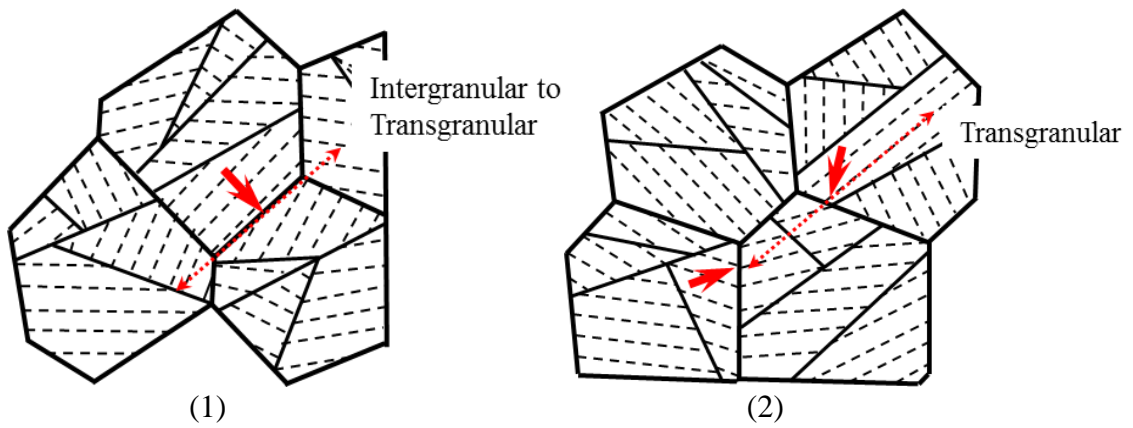
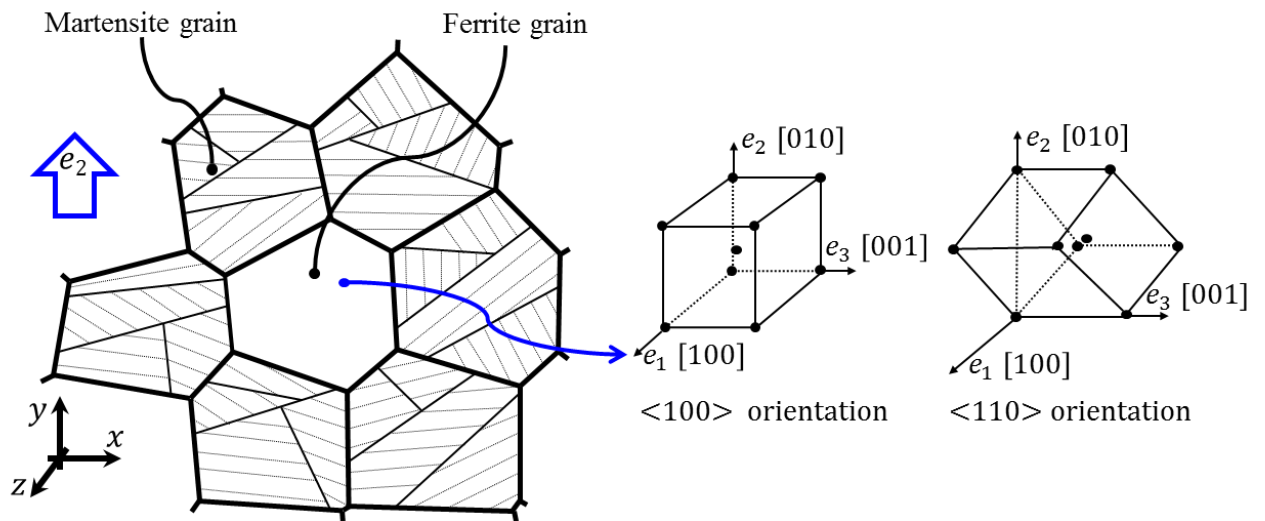
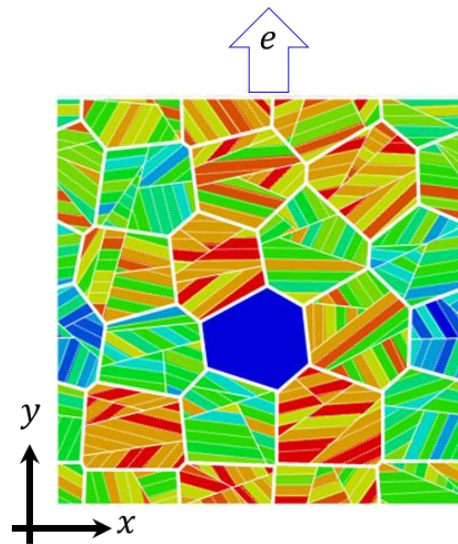


Fig. 12: Schematic illustration of micro-cracking propagation of two main cracks from Fig. 11(b) for single phase (5.5% strain) at 10^{-3} /s strain-rate.



(a)



(b)

Fig. 13: (a) Isolated ferrite grain embedded within a martensite matrix and two ferrite orientations chosen for ferrite grain in mixed-phase. (b) Micromechanical finite element model for mixed-phase with a small amount of ferrite.

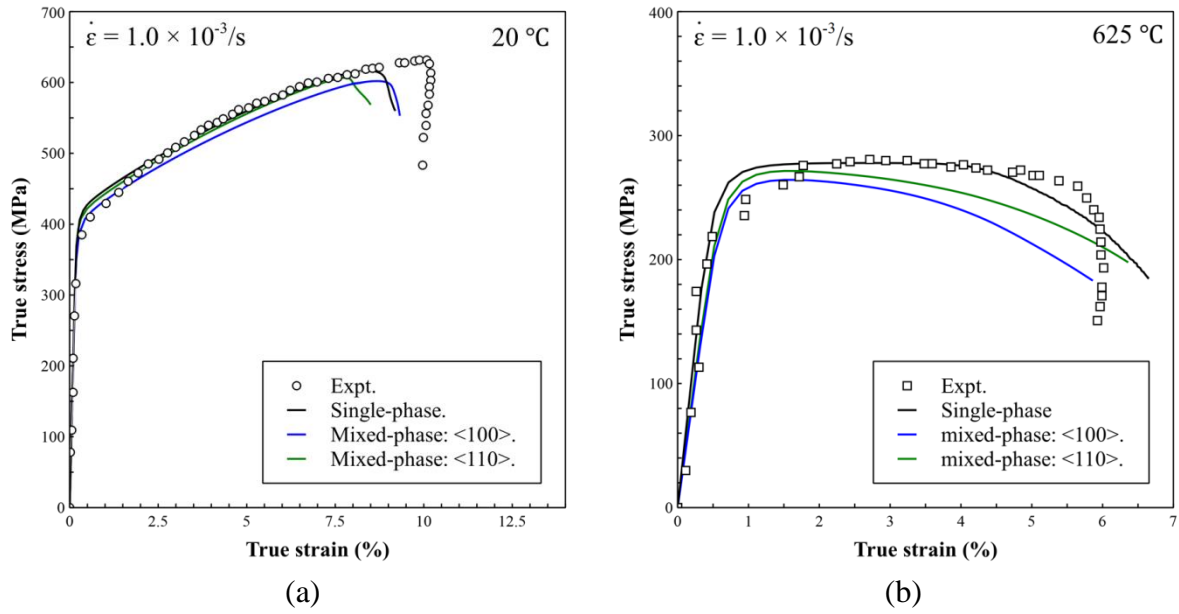


Fig. 14: Comparison of CPFE-predicted results at 20 °C and 625 °C (a) Predicted single-phase and mixed-phase responses correlated to the measured IC-HAZ stress-strain data 20 °C; (b) Predicted single-phase and mixed-phase responses correlated to the measured IC-HAZ stress-strain data 625°C.

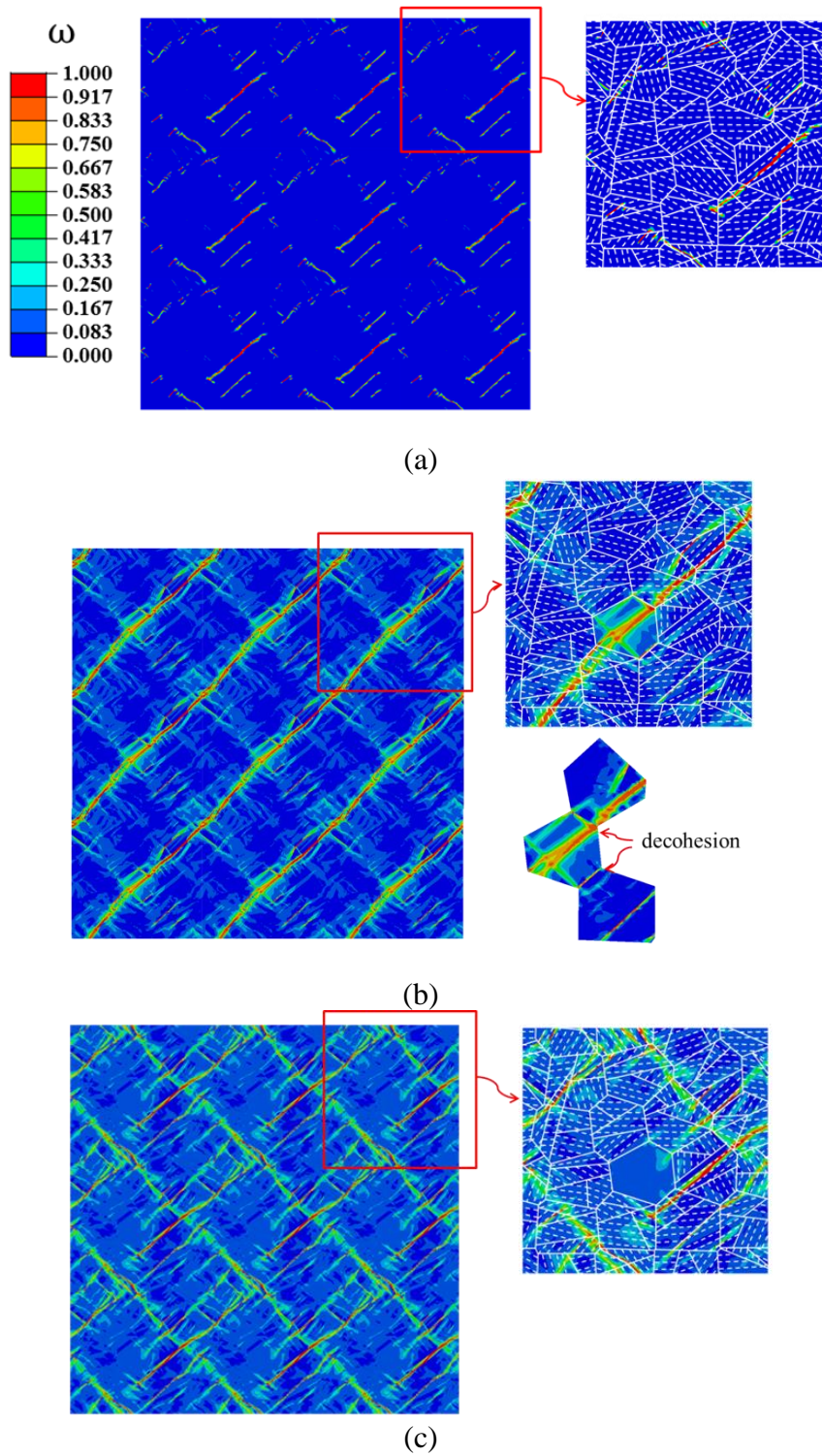


Fig.15: Prediction of micro-crack evolution for the single-phase and mixed-phase at 625 °C with 20% drop load, (a) Single-phase at 6% strain; (b) mixed-phase with $\langle 100 \rangle$ at 5.1% strain; (c) mixed-phase with $\langle 110 \rangle$ at 5.75% strain;